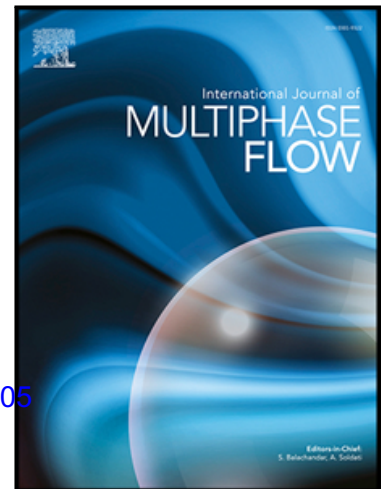


Journal Pre-proof

Primary breakup regimes for cryogenic flash atomization

D.D. Loureiro, J. Reuttsch, A. Kronenburg, B. Weigand,
K. Vogiatzaki

PII: S0301-9322(20)30514-0
DOI: <https://doi.org/10.1016/j.ijmultiphaseflow.2020.103405>
Reference: IJMF 103405



To appear in: *International Journal of Multiphase Flow*

Received date: 19 March 2020
Revised date: 2 June 2020
Accepted date: 19 June 2020

Please cite this article as: D.D. Loureiro, J. Reuttsch, A. Kronenburg, B. Weigand, K. Vogiatzaki, Primary breakup regimes for cryogenic flash atomization, *International Journal of Multiphase Flow* (2020), doi: <https://doi.org/10.1016/j.ijmultiphaseflow.2020.103405>

This is a PDF file of an article that has undergone enhancements after acceptance, such as the addition of a cover page and metadata, and formatting for readability, but it is not yet the definitive version of record. This version will undergo additional copyediting, typesetting and review before it is published in its final form, but we are providing this version to give early visibility of the article. Please note that, during the production process, errors may be discovered which could affect the content, and all legal disclaimers that apply to the journal pertain.

© 2020 Published by Elsevier Ltd.

Highlights:

- Multi-phase DNS captures the primary breakup dynamics in flash-boiling atomization
- A calibration model correlates superheat level to Weber and Ohnesorge numbers
- Systematic classification of distinct droplet formation mechanisms
- Relevant flow dynamics are observed that are currently neglected by existing models

Journal Pre-proof

Primary breakup regimes for cryogenic flash atomization

D. D. Loureiro^a, J. Reutzsch^b, A. Kronenburg^{a,*}, B. Weigand^b, K. Vogiatzaki^c

^a*Institute for Combustion Technology, University of Stuttgart, Germany*

^b*Institute of Aerospace Thermodynamics, University of Stuttgart, Germany*

^c*Advanced Engineering Centre, University of Brighton, UK*

Abstract

Flash boiling atomization can occur in rocket thrusters operating in the vacuum of space when the cryogenic liquid propellants are injected into the reaction chamber just before ignition. The sudden drop in pressure triggers the nucleation of microscopic vapour bubbles that grow in the superheated liquid, leading to extreme jet expansion and atomization. Direct numerical simulations are performed using the multiphase solver FS3D to bring insight into the primary atomization process occurring at the microscopic level. The code uses the volume of fluid method and PLIC reconstruction to track the liquid-vapour interface with high fidelity, fully resolving viscous and capillary effects. An incompressible scheme is used, yet all the relevant thermodynamic effects associated with flash boiling are considered by calibration of the evaporation rate and fluid properties based on exact solutions for bubble growth in superheat liquid. A series of test cases with regular bubble arrays demonstrates how the initial bubble spacing and liquid temperature can be correlated to a range of Weber and Ohnesorge numbers. This allows for the definition of very distinct breakup mechanisms and resulting droplet patterns. These extend beyond the common assumptions used in the literature to estimate the primary droplet size and indicate a range of possible droplet size distributions depending on the breakup regime.

*Corresponding author

Email address: kronenburg@itv.uni-stuttgart.de (A. Kronenburg)

Keywords: Multi-phase DNS, Bubble Growth, Flash Boiling Atomization, Cryogenic Propellants

1. Introduction

Flash boiling occurs when a pressurized liquid is rapidly discharged into an environment where the pressure is below the liquid's saturation pressure. The liquid becomes superheated and experiences a sudden phase change that is triggered by spontaneous nucleation of a large number of microscopic vapour bubbles that rapidly grow and coalesce leading to a wide spray of very fine droplets. These conditions are generally beneficial for liquid atomizers and can be found in various applications from common household aerosol cans, to state-of-the-art fuel injection systems such as gasoline direct injection (GDI) and rocket engines, with the latter being the main motivation for this work. Nonetheless, it is also an important effect to consider in hazardous situations, such as steam explosions, failure of rocket engine fuel lines or nuclear accidents. Flash boiling in rocket engine injectors becomes relevant in upper stage engines that require high reliability of ignition and combustion stability, as well as in reaction control systems (RCS) where frequent ignitions are performed for high precision orbital maneuvering and attitude control. To simplify the spacecraft design and improve ground handling safety and costs, there is a trend 1) to replace toxic hydrazine-based propellants with cryogenic alternatives such as LH2-LOx or LCH4-LOx, and 2) to eliminate the use of igniter fluids with the use of sparks and focused lasers (Manfretti, 2014; Hurlbert et al., 1998). Although the injection conditions rapidly change as soon as the engine is ignited, the reliability of the ignition is highly dependent on the initial spray morphology and the quality of the propellant mixing. This has motivated research on the injection of cryogenic liquids in vacuum conditions (Lecourt et al., 2009; Manfretti, 2014; Lamanna et al., 2015; Rees et al., 2019), primarily using experimental methods.

Comprehensive studies on flash boiling can be found in Sher et al. (2008), Lamanna et al. (2014) and Bar-Kohany and Levy (2016). It is well established

that the morphology of a flashing spray is primarily determined by the level of superheat, which can be controlled by the liquid temperature and the chamber pressure. In fully flashing conditions, which naturally occur in a near-vacuum environment, the breakup is directly driven by phase change as vapour bubbles nucleate and grow within the liquid. In this regime, very wide jet spreading angles are typically observed as the jet is instantly atomized into microscopic droplets with high radial velocity. While several successful models and engineering tools have been developed in the last century for aerodynamic breakup (Ashgriz, 2011), the current understanding of flash boiling breakup is rather limited. Various empirical correlations exist for the estimation of the spray characteristics across the range of flashing conditions (Lamanna et al., 2015; Luo and Haidn, 2016; Cleary et al., 2007; Levy et al., 2014). These studies generally rely on high-speed shadowgraphy or Schlieren imagery for the spray morphology or laser based methods such as Phase Doppler Anemometry (PDA) to obtain statistics on droplet sizes and velocities. However, they cannot provide insight into the microscopic breakup process inside or near the exit of the nozzle, where the spray is extremely dense and optical access is limited. For this reason any model for the underlying primary breakup process remains somewhat hypothetical.

Excluding aerodynamic effects, some of the breakup mechanisms suggested for fully flashing conditions are bubble coalescence and micro explosion (Oza and Sinnamon, 1983). Bubble coalescence is assumed by Sher and Elata (1977), Senda et al. (1994) and various subsequent works for very high nucleation rates. They further hypothesise that the bubbles are arranged in a close-packed cubic array, resulting in a number of droplets that is exactly double the original number of bubbles per unit volume. Then, their size can be estimated based on a critical volume fraction that is empirically calibrated. The micro explosion regime is covered in works such as Razzaghi (1989) and Zeng and Lee (2001). These pertain to the particular case of secondary breakup due to bubble nucleation and growth within previously detached droplets. The micro explosion regime is still driven by bubble nucleation and growth in the interior of the

droplet, so the bubble coalescence regime still applies, except at the outermost
60 interface. While these models can be useful for the development of engineering
tools for flash atomization, they continue to rely on empirical correlations
and have limited predictive capabilities. Furthermore, the microscopic droplet
formation mechanisms have never been directly observed or simulated.

In the face of these limitations as well as the costs associated with experimen-
65 tal studies for cryogenic propellants, numerical approaches become attractive
alternatives. However, due to the wide range of length and time scales involved
in flash boiling atomization, it becomes infeasible to perform fully coupled CFD
simulations of the complete liquid spray while resolving bubble nucleation and
growth. The problem can instead be divided into three domains according to the
70 scales and physics involved: i) bubble growth in a superheated liquid, ii) bubble
coalescence and droplet formation and iii) macroscopic flow spray morphology.
At the microscale, the dynamics of bubble growth are well documented in the
literature using theoretical and numerical methods and validation of these meth-
ods by experiments (Lee and Merte, 1996; Robinson and Judd, 2004; Sher et al.,
75 2008; Prosperetti, 2017). At the opposite end, the macroscale, numerous studies
investigate large scale characteristics such spray density, breakup, spreading an-
gle and penetration (cf. Lee et al. (2009), Navarro-Martinez (2014), Karathanas-
sis et al. (2017), Gaertner et al. (2019, 2020), Calay and Holdo (2008)). None of
the methods used, however, is able to capture the breakup process which occurs
80 at the sub-grid scale and, so far, rely on empirically calibrated models for the
phase change process that is - in turn - dependent on the surface area density
of the spray.

The present work attempts to bridge the gap between the small and large
scales. We use multiphase DNS for the investigation of the microscopic flashing
85 spray dynamics. The approach resolves the liquid vapour interface to simulate
the breakup process when multiple bubbles in a cluster coalesce and burst. This
provides novel insights into the dynamics of droplet formation in flash atom-
ization conditions, and a classification of distinct breakup patterns as function
of the local thermodynamic conditions can be identified. We focus here on the

90 hydrodynamics of the breakup process, i.e., the dynamics governed by the ef-
fects of viscous and capillary forces acting against the liquid momentum change
driven by bubble expansion. As the DNS cannot cover the entire flashing jet
and its surroundings, care must be taken with the setup of the cases respecting
local thermodynamic conditions (pressure and temperature), heat transfer and
95 compressibility effects that determine the bubble growth rates and fluid proper-
ties at various stages of bubble growth. It is noted that the current DNS faces
the standard limitations with respect to model validation that is inherent in the
DNS approach. Experimental techniques do not allow for measurements of the
small-scale dynamics from bubble nucleation towards jet disintegration under
100 cryogenic flash atomization conditions. Only full scale large-eddy simulation
(LES) would allow for such direct validation with experiments, and the current
DNS shall therefore provide insight into the dynamics of small scale hydrody-
namics during bubble growth that can then be used for modelling the sub-grid
processes that lead to jet expansion, breakup and droplet formation.

105 This paper is therefore organized as follows: In Sec. 2, the simulation domain
is defined in relation to a relevant experimental configuration and the parameters
that affect the flashing dynamics are introduced. In Sec. 3 we describe the
dynamics of bubble growth using first-principle models from the literature. In
Sec. 4 the numerical schemes and methods of the DNS are detailed. In Sec. 5
110 we characterize different breakup regimes in terms of characteristic numbers.
These can then be used to estimate the resolution requirements and to construct
a reference diagram to classify the breakup patterns observed for each case. The
cases are grouped by breakup regimes and individually analysed in Sec. 6. In
Sec. 7, the assumptions and approximations made in this work are summarised
115 to discuss the direction of future studies. Finally, in Sec. 8 the main conclusions
are presented.

2. Investigated configuration

In this work we focus on the small scale spray dynamics and select a computational domain that represents a small control volume within a flashing jet. We present one possible context for the set-up such that the choice of parameters and the physics involved can be better understood. However, the results are relatively independent of the large scale characteristics of the jet (as will be seen in Sec. 5). They are largely determined by the local thermodynamic properties and the findings should be applicable to any configuration where - locally - the same set of thermodynamic conditions determine bubble nucleation and growth.

We consider a cryogenic liquid initially stored at subcooled conditions (temperature T_ℓ and pressure p_0) that is released through an injector nozzle into a low pressure combustion chamber. Liquid oxygen (LOx) is selected as the working fluid and the range of conditions simulated here is related to corresponding experiments at the Institute of Space Propulsion of DLR Lampoldshausen (Lamanna et al., 2015; Rees et al., 2019) such that resulting droplet size distributions from the DNS may be used as submodels for LES of the entire flash-boiling experiment. In the experiments, the injection temperatures are between 80 K and 120 K and initial chamber pressures can be varied with the lowest pressures being 1000 Pa.

Depending on the injector design, different flow structures can be expected (cf. Thompson and Heister (2016) or Bar-Kohany and Levy (2016)). The schematic of Fig. 1 depicts one possible flow pattern with various internal vaporization processes, as well as a hypothesized pressure profile for a choked two-phase flow. At the exit of the nozzle a steep pressure drop is expected towards the environment chamber pressure. In the experiments, extremely wide spray angles can be observed for high superheat levels. This indicates that radial jet expansion and the final atomization must be driven by sudden bubble growth starting when the fluid enters the low pressure chamber. As the DNS domain cannot cover the entire flash-boiling jet we now focus on a small volume of liquid near the exit of the injector nozzle (or within a large liquid structure further downstream) where bubble growth is expected to dominate the breakup

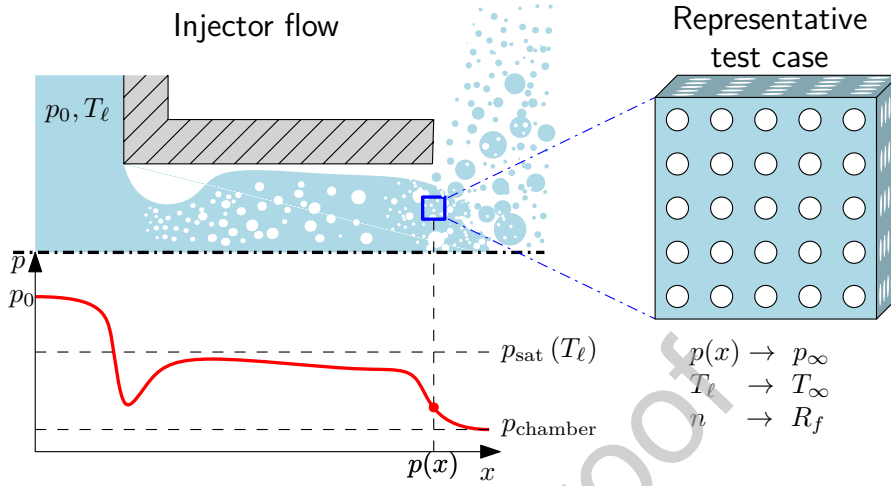


Figure 1: Schematic of the injector flow with internal bubble formation and hypothesised pressure profile given as context for the definition of the DNS test case.

dynamics. The DNS domain is also shown in Fig 1.

The local pressure within the jet is taken as the environment pressure for the test case, p_∞ . Similarly, the far-field liquid temperature in the DNS domain, T_∞ , corresponds to the local liquid temperature. Although these can take a range of values that are unknown a priori, it can be assumed that p_∞ is close to the chamber pressure, and T_∞ matches the liquid temperature in the reservoir. Since the injection mass flow rate and the precise locations of bubble nucleation are not known (the first bubbles responsible for the atomization may even have nucleated upstream) we do not attempt to estimate a local nucleation rate (Lamanna et al., 2014). Instead, the local bubble number density, n , is treated as a free parameter and the test cases are populated with arrays of uniformly spaced bubbles. The domain emulates a fluid element moving with the jet velocity. At the time of nucleation, any volumetric displacement by the emerging (small) nuclei is negligible. The liquid is not accelerated, and the relative velocity between the bubbles and the surrounding liquid is therefore set to zero initially. Further, no velocity gradients in the liquid are imposed, i.e. we assume the control volume to be sufficiently small and to be located sufficiently far away

from the injector walls. Bubble growth then leads to a relative acceleration of the bubbles towards each other, to the development of shear layers in the liquid and relative velocities between bubbles and surrounding liquid. The dynamics of this bubble expansion process are the only driving force for the breakup and fully captured by the DNS. A cubic lattice arrangement has been chosen in the present study to simplify the setup process and analysis (see also discussion in Sec. 7). The bubble size at time of coalescence and the bubble number density are not independent quantities as the initial distance determines how much the bubbles will grow until they touch and the breakup process starts. We therefore define the parameter R_f as the final bubble radius at which the bubbles are expected to merge. In the limit of an infinitesimally small nucleation kernel and a high density ratio between liquid and vapour, the relation

$$n = \left[R_f^3 \left(8 - \frac{4\pi}{3} \right) \right]^{-1} \quad (1)$$

150 can be derived for the cubic lattice arrangement. The thermodynamic conditions (p_∞ and T_∞) determine the evolution of the fluid properties for both phases as well as the bubble growth rate from nucleation to the time when the bubbles merge. These are calculated for each case based on a model for bubble growth in a superheated liquid which is detailed in the next section.

155 3. Bubble nucleation and growth

DNS of the hydrodynamics of flash atomization of pure liquids do not implicitly capture the phase transfer at the interface between vapour and liquid as this is a molecular process, and models are needed for closure (Dietzel et al., 2019b). An overview of the dynamics of bubble nucleation and growth can be
 160 found in various reviews including Lee and Merte (1996), Sher et al. (2008) and Prosperetti (2017). Their treatment is based on classical theory and neglects some molecular-scale effects, for a more detailed theory see Oxtoby (1992), Shusser et al. (2000) and Shneider and Pekker (2019). The phase change diagram in Fig. 2 shows the vaporization process for a liquid initially stored at

165 sub-cooled conditions (point A) that is isothermally released into a low pressure environment at p_∞ (point B). Point B is below the saturation line such that the liquid is in a meta-stable superheated condition. The liquid can remain temporarily in this state, until local fluctuations of density or pressure or a nucleation site trigger the phase change process. Considering the liquid tem-

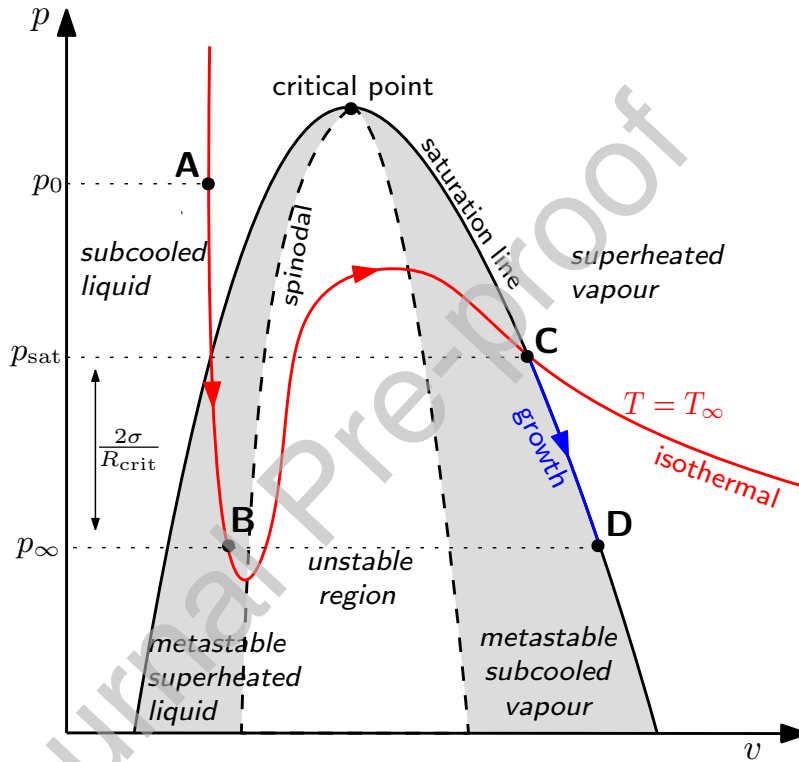


Figure 2: Schematic of the phase change process along the pressure-volume isotherm, showing liquid superheating (A-B), isothermal nucleation (B-C) and bubble growth (C-D).

170 perature, T_∞ , and the environment pressure, p_∞ , the saturation temperature $T_{\text{sat}}(p_\infty)$ is the reference stable state for the liquid phase, while the saturation pressure $p_{\text{sat}}(T_\infty)$ defines the new stable condition for the vapour (point C). These can be used to define the level of superheat as $\Delta T = T_\infty - T_{\text{sat}}(p_\infty)$ or the pressure ratio $R_p = p_{\text{sat}}(T_\infty)/p_\infty$. Thus, a spontaneous nucleation can occur
175 without additional heat being supplied leading to a transition from state B to

state C, approximating an equilibrium phase change process where the vapour pressure in the bubble nucleus is given by $p_v = p_{\text{sat}}(T_\infty)$. This corresponds to the most common approximation for p_v and is compatible with the solution of the Rayleigh-Plesset equation as described below, but other assumptions are possible. Full thermodynamic equilibrium between liquid (point B) and vapour would require point C to lie within the superheated vapour regime (Carey, 1992; Ashgriz, 2011). Differences in vapour pressure tend to be small (between 0.01% for $T=80$ K and 3.4% for $T=120$ K), and we therefore choose $p_v = p_{\text{sat}}(T_\infty)$ for consistency with further modelling using the Rayleigh-Plesset equations.

Based on the Young-Laplace equation, we then define the critical bubble radius, R_{crit} , for which the pressure difference is in mechanical equilibrium with the surface tension, by

$$R_{\text{crit}} = \frac{2\sigma}{p_{\text{sat}}(T_\infty) - p_\infty}, \quad (2)$$

where σ is the surface tension coefficient at T_∞ . Nuclei smaller than R_{crit} cannot be formed as they would collapse under the surface tension force, while larger ones will experience rapid growth due to reduced surface tension paired with continuous evaporation of liquid at the interface.

The conditions inside the bubble follow the saturation line as the bubble grows towards the state indicated by point D. The entire process can be characterized by the Jakob number which quantifies the ratio between the available heat stored in the liquid and the latent heat required for vaporization. It is defined by (e.g. Prosperetti (2017)):

$$\text{Ja} = \frac{\rho_\ell C_{p,\ell} |T_\infty - T_{\text{sat}}(p_\infty)|}{\rho_v h_{\text{fg}}}, \quad (3)$$

where ρ_v is the vapour density at $T_{\text{sat}}(p_\infty)$, $C_{p,\ell}$ is the specific heat of the liquid and h_{fg} is latent heat of evaporation, both evaluated for the superheated liquid with p_∞ and T_∞ .

With the assumption of spherical symmetry, the growth (or collapse) of a vapour bubble is governed by the Rayleigh-Plesset equation (see eg. Lee and

Merte (1996) and Sher et al. (2008))

$$R\ddot{R} + \frac{3}{2}\dot{R}^2 = \frac{1}{\rho_\ell} \left(p_v - p_\infty - \frac{2\sigma}{R} - \frac{4\mu_\ell}{R}\dot{R} \right). \quad (4)$$

The vapour pressure p_v becomes the driving force that accelerates the surrounding liquid against the opposing forces of the environment pressure, surface tension and viscosity, respectively. Nuclei larger than R_{crit} will grow exponentially as the surface tension becomes negligible and the pressure differential is balanced only by the liquid inertia and viscosity. This is referred to as the *inertia controlled* stage of growth (Sher et al., 2008). During this process, the saturation condition is maintained by continuous evaporation at the interface. However, due to the supply of latent heat of evaporation, the temperature of the interface, T_Γ , will start to decrease forming a thermal boundary layer around the bubble. As T_Γ decreases, so does the vapour pressure, following the saturation line with $p_v = p_{\text{sat}}(T_\Gamma)$ as represented by the blue line in Fig. 2. The bubble growth decelerates until a new equilibrium is reached with $T_\Gamma = T_{\text{sat}}(p_\infty)$ and $p_v = p_\infty$ (point D). At this point the growth is governed by the supply of thermal energy through conduction from the surrounding liquid to the interface and is referred to as the *thermal diffusion controlled* stage of growth. Several approximate models can be found in the literature to model both stages of bubble growth. In this work the numerical method of Lee and Merte (1996) is used as a reference. They integrate the Rayleigh-Plesset equation in time, considering the saturation condition $p_v = p_{\text{sat}}(T_\Gamma)$ and taking into account variation of fluid properties with temperature. The interface temperature, T_Γ , is obtained by additionally solving the energy transport equation in spherical coordinates with a full resolution of the thermal boundary layer surrounding the bubble. The boundary condition at the interface ensures that the heat flux matches the latent heat of evaporation. On the vapour side the temperature is assumed uniform and equal to T_Γ . The saturation condition and the fluid properties are evaluated using the open source library CoolProp (Bell et al., 2014). The coupled solution of the Rayleigh-Plesset and energy equations have emerged as one set of preferred model equations as firstly, modern computer resources renders their solution in-

Table 1: Superheat and critical radius for Oxygen at $p_\infty = 1000$ Pa

T_∞	80 K	100 K	120 K
ΔT	18.71	38.71	58.71
R_p	30.12	254	1022
Ja	2511	4920	7463
$R_{\text{crit}}(\text{m})$	1.081×10^{-6}	8.487×10^{-8}	1.202×10^{-8}

220 expensive and secondly, the method is able to capture the continuous transition between the equilibrium state at the critical radius, the inertia controlled stage and the thermal diffusion controlled stage while the bubble radius increases by several orders of magnitude. It will be used as a reference throughout this work and referred to as RP-e (Rayleigh-Plesset + energy) for brevity.

225 Solving the RP-e equations, a database can be built for a given working fluid and each ambient condition (given by p_∞, T_∞ from the DLR LOx experiments). The database specifies the bubble growth rate, \dot{R} , and other temperature dependent variables (ρ_v, σ , etc.) that can be tabulated as functions of the bubble size. Table 1 provides the corresponding levels of superheat and Jakob number as well as critical radii for some selected cases used in this study.

230 The results are shown in Fig. 3 where the independent variable is the normalized radius $R^* = R/R_{\text{crit}}$ representing the growth factor since nucleation. The solid lines correspond to the solution for $p_\infty = 1000$ Pa, primarily used in this work, while the dashed lines correspond to $p_\infty = 10^5$ Pa to show the relative influence of p_∞ . Several observations can be made: First, it seems that the peak in growth rate is consistently reached when the bubble has grown by a factor between 10 and 20, justifying the use of R^* as a reference variable. The subsequent decrease in \dot{R} is due to cooling of the interface showing that the transition stage, where both inertia and heat diffusion are important, is quite extended. The heat diffusion stage, where $T_\Gamma = T_{\text{sat}}(p_\infty)$, is not reached for most cases within the ranges shown here. The exception is the case with $T_\infty = 80$ K, $p_\infty = 10^5$ Pa (dashed green line) where an inflection point can be

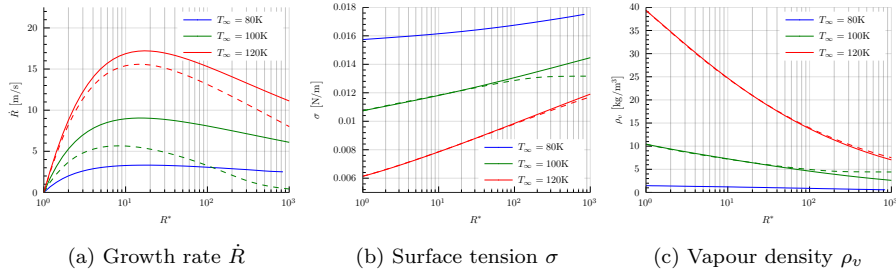


Figure 3: Results of the spherical bubble growth model (RP-e) as function of relative bubble size $R^* = R/R_{\text{crit}}$ for the range of liquid temperatures T_∞ (80 K to 120 K) and pressures $p_\infty = 10^3$ Pa (solid lines) and $p_\infty = 10^5$ Pa (dashed lines).

observed. Nonetheless, as the bubble grows during the inertial stage, the variation of surface tension, σ , and vapour density, ρ_v , is significant for all cases. This highlights the importance of an adequate representation of these quantities as a function of bubble size, and near-equilibrium conditions (i.e., $p_v = p_{\text{sat}}(T_\infty)$ or $T_\Gamma = T_{\text{sat}}(p_\infty)$) do certainly not hold even if equilibrium is often used as a standard in the literature (Bardia and F. Trujillo, 2018). The RP-e solutions also show a small influence of p_∞ for the range of conditions investigated here. For this reason, although p_∞ is one of the three free parameters, we only focus on the cases with $p_\infty = 10^3$ Pa (higher superheat levels) where fully flashing flows are expected.

The RP-e model covers the complete growth of individual bubbles in flashing conditions. It does not, however, take into consideration any interactions between the bubbles, in particular how they deform, merge and burst to form the spray. This can only be captured in full 3D simulations that resolve the hydrodynamics of bubble dynamics as is suggested here. The RP-e model is then only used for calibration of the initial conditions and the modelling of the mass transfer rate.

260 4. Numerical Methods for 3D Bubble Arrays

In this section, we describe the numerical methods used for the 3D DNS simulations of the breakup process. In Sec. 4.1 we give the general governing equations and provide detail on the treatment of the two-phase flows. In Sec. 4.2, we define the specific DNS setup including the initial and boundary conditions.

265 4.1. Governing equations

The in-house code Free-Surface 3D – FS3D (e.g. Eisenschmidt et al. (2016)) is used for the DNS of the atomization process. The code solves the incompressible Navier-Stokes equations, while capturing a sharp liquid-vapour interface with phase change and surface tension using the volume of fluid (VOF) method with PLIC (piecewise linear interface calculation) reconstruction. The Navier-Stokes equations are formulated using a one-fluid approach for a continuous velocity, \mathbf{u} , and pressure field, p , yielding

$$\frac{\partial}{\partial t} (\rho \mathbf{u}) + \nabla \cdot [\rho \mathbf{u} \mathbf{u}] = \nabla \cdot \mu \left[\nabla \mathbf{u} + \nabla (\mathbf{u})^T \right] - \nabla p + \mathbf{f}_\sigma, \quad (5)$$

where $\mathbf{u} \mathbf{u}$ is a dyadic product. Buoyancy forces have been neglected, and \mathbf{f}_σ denotes the effects of surface tension. The latter is non-zero at the interface and modeled by the continuum surface stress (CSS) model (Lafaurie et al., 1994). In the VOF method an additional variable is transported representing the volume fraction of liquid in the cell, f , with $f = 1$ in the liquid phase, $f = 0$ in the gas phase and $0 < f < 1$ in cells containing the interface. Volume-averaged properties are then defined as $\rho = \rho_\ell f + \rho_v (1 - f)$ for the density and $\mu = \mu_\ell f + \mu_v (1 - f)$ for viscosity, where the subscripts ℓ and v denote the liquid and vapour phases. The volume fraction transport equation can be written as (Schlottke and Weigand, 2008)

$$\frac{\partial f}{\partial t} + \nabla \cdot (f \mathbf{u}_\Gamma) = \frac{\dot{m}'''}{\rho_\ell}, \quad (6)$$

where \mathbf{u}_Γ is the interface velocity and \dot{m}''' is the liquid evaporation rate at the interface. The latter can be defined as $\dot{m}''' = a_\Gamma \dot{m}''$, using the evaporation mass

flux, \dot{m}'' , and the interface density, a_Γ , which represents the interface area per unit volume. The pressure field, p , is obtained by solving the pressure Poisson equation

$$\nabla \cdot \left[\frac{1}{\rho} \nabla p \right] = \frac{\nabla \cdot \mathbf{u}}{\Delta t}, \quad (7)$$

using an efficient multi-grid method (Rieber, 2004). Continuity is implied in the velocity divergence term with $\nabla \cdot \mathbf{u} = 0$ except in interface cells (with $0 < f < 1$). There, $\nabla \cdot \mathbf{u}$ is determined to account for phase change with large density ratio as a function of the evaporation rate, \dot{m}'' , using the method
 270 detailed in Schlottke and Weigand (2008) which ensures mass conservation in spite of a volume averaged density being used. This naturally introduces the jump condition in the momentum conservation equation through p . The system of equations is discretized on a uniform Cartesian mesh using the finite volume method in a staggered grid. A second order upwind scheme is used for the
 275 advective terms and second-order central difference for the diffusive terms. The time integration is done using a first order Euler explicit scheme.

A PLIC scheme (Rider and Kothe, 1998) is used to determine an interface plane in each cell and a_Γ , thus maintaining a sharp interface. Coupled with the CSS model this is a flexible approach that requires only moderate resolution
 280 when modeling bubble coalescence, liquid breakup and droplet collisions. However, non-physical dynamics can be introduced at very low resolutions leading to mesh dependent effects (Liu and Bothe, 2016). The implication with respect to mesh resolution are further analysed in Secs. 5.2 and 6.

While DNS resolves all hydrodynamically important scales, it cannot capture the molecular processes at the interface that determine the evaporation rate. Phase change, given by the unknown \dot{m}'' , as well as the vapour properties (ρ_v , μ_v) and surface tension coefficient, which depend on the temperature of the interface, are taken from the RP-e method for the thermodynamic conditions p_∞ and T_∞ and for the final bubble size, R_f (see Sec. 3). Thus, we define the evaporation mass flux

$$\dot{m}'' = \rho_v \dot{R}, \quad (8)$$

which determines the jump condition at the interface, with \dot{R} acting as an
 285 imposed interface velocity relative to the bubble centre. All the fluid properties
 and the evaporation rate are kept constant throughout the breakup process
 which is consistent with the use of an incompressible solver. Thus, bubble
 interactions are only captured in terms of fluid transport and the effects of
 propagating pressure waves or liquid cooling are neglected. The hydrodynamics
 290 effects are expected to dominate the breakup process, but possible consequences
 and solutions for the approximations used here are further discussed in Sec. 7.

4.2. Initialization and boundary conditions

Figure 4 depicts the calculation domain of the DNS. The liquid is free to
 expand through the use of continuity boundary conditions (outflow) and large
 buffer zones are used to represent the inertia of the surrounding liquid. *As the
 computational domain represents a fluid volume with homogeneous thermody-
 namic conditions bubbles would also form in the buffer zones. However, these
 bubbles are omitted here as (i) they would be pushed off the domain and would
 not contribute to the final analysis, (ii) the presence of fragments of bubbles
 and interstitial liquid at the bounds makes the analysis of droplet characteris-
 tics ambiguous and (iii) the interaction of the liquid-vapour interface with the
 boundaries may lead to computational instabilities.* Symmetry conditions are
 used to reduce the computational costs. The same view depicted in Fig. 4 will
 be used later in Sec. 6 for the visualization of the simulation results. Since con-
 stant density is assumed in each phase, mass conservation can be used to derive
 the initial bubble spacing, D_i , that will lead to bubble merging at R_f giving

$$D_i = R_f \sqrt[3]{8 - \frac{4\pi}{3} \left(1 - \frac{\rho_v}{\rho_\ell}\right) \left(1 - \frac{R_i^3}{R_f^3}\right)} \quad (9)$$

for a cubic droplet lattice. Here, the initial bubble radius, R_i , is equal to the
 maximum of the critical radius and usually around 20% of the final radius, $R_i =$
 295 $\max(R_{\text{crit}}, 0.2R_f)$. This ensures the vast majority of bubble volume expansion
 to be covered by the simulation before bubble coalescence starts while avoiding

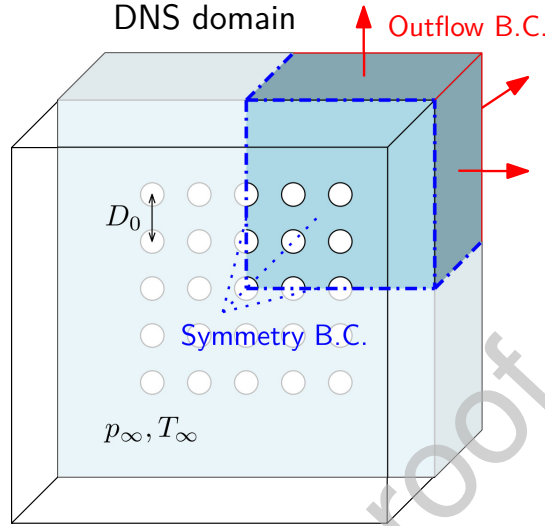


Figure 4: DNS domain setup with boundary conditions

the need for mesh resolutions beyond the requirements needed for the breakup process. While D_i and R_i are required to define the simulation domain, the fluid-dynamics of the breakup should depend only on the bubble size, R_f , growth rate, \dot{R} , and the fluid properties. As \dot{R} and the fluid properties are functions of p_∞ , T_∞ and R_f (as given by the RP-e solution - see Sec. 4.1), these three parameters fully characterize the flow.

Simulations are performed for $T_\infty = 80, 100$ and 120 K, and $R_f^* = 2, 5, 10$ and 50 . Here, R_f^* denotes R_f normalized by the critical radius R_{crit} . R_f^* represents the bubble growth from nucleation until bubble coalescences starts. The range of R_f^* values implies that bubble merging occurs in the early stages of growth as would be expected for high levels of superheat and fully flashing sprays. The range between 2 and 50 may appear limited but it is equivalent with a 4 orders of magnitude variation for the equivalent bubble number density as given by Eq. 1 (or 8 orders of magnitude across all R_f^* and T_∞ cases). Only $p_\infty = 1000$ Pa has been considered due to the pressure's small influence on this stage of growth as observed in Sec. 3. Each setup represents a cluster with 125 bubbles exploiting symmetry conditions as indicated in Fig. 4. The bubble positions are determined

by Eq. 9 but enforcing the exact bubble distances that are aligned with the mesh
 315 and the grid size can lead to unrealistic results and obscures the real physics.
 Therefore, a random offset of the bubble centers is introduced. This offset does
 not exceed a maximum of $0.1R_f$ and does not significantly change the overall
 instant of coalescence or the actual size of bubbles when they merge.

5. Flow characterization

320 Different bubble number densities (nucleation rates) imply different final
 bubble sizes at the time of coalescence. The calibration with the RP-e solution
 then provides different fluid properties and evaporation rates leading to different
 relative strengths of the forces involved when bubbles merge. This can be used
 for a preliminary characterization of the breakup patterns as well as determining
 325 the resolution requirements. The former is detailed in Sec. 5.1 while the latter
 will be discussed in Sec. 5.2.

5.1. Breakup dynamics

The dynamics of liquid breakup processes are typically characterized by the
 Weber and Ohnesorge numbers. Here, we use final bubble diameter, $2R_f$, and
 the interface velocity, \dot{R} , as characteristic scales to define

$$\text{We}_b = \frac{2R_f \rho_\ell \dot{R}^2}{\sigma}, \quad (10)$$

where the subscript b refers to a single bubble (as opposed to conventional
 droplet related definitions of these characteristic quantities). As such, We_b
 represents the relative strength of the bubble surface tension force against liquid
 momentum due to bubble expansion. Similarly, the Ohnesorge number can be
 defined as

$$\text{Oh}_b = \frac{\mu_\ell}{\sqrt{2R_f \rho_\ell \sigma}}, \quad (11)$$

to represent the strength of viscous dissipation (in the liquid) against the prod-
 uct of liquid inertia and surface tension. These definitions are used to locate
 330 the computed cases in the Weber-Ohnesorge diagram as shown in Fig. 5. Using

the RP-e solution, We_b and Oh_b are calculated for selected T_∞ (80K, 100K and 120K) over a continuous range of R^* providing the solid, near horizontal lines. The dashed lines connect points of equal R^* and correspond to the R_f^* selected for DNS. This procedure leads to a series of 12 DNS cases that was simulated
 335 with geometrically identical setups and equal mesh resolution. The results of the DNS then provided a preliminary classification of the breakup patterns or modes (Loureiro et al., 2018). These preliminary results were then used to define the resolution requirements and other setup parameters, such as the size of the buffer zone and the offset on the initial bubble positioning in the otherwise
 340 regular array. The final classification distinguishes three regimes as indicated in Fig. 5: the retracting liquid regime, the ligament stretching regime and the thin lamella regime, where the ligament stretching regime can be sub-divided into regimes with and without formation of satellite droplets. The overlap of the latter regimes highlights the fact that the mechanics associated with each of
 345 these can be observed simultaneously or during different stages of the breakup process. Qualitative results will be shown for selected cases (labelled by letters A to G) which are analysed in detail in Sec. 6 and serve as explanation for the given classifications. For the selected cases, the physical parameters, dimensionless numbers and other setup variables are summarized in Table 2.

350 5.2. Resolution requirements

DNS of multiphase flows implies that the smallest liquid structures and interface instabilities are fully resolved. However, DNS of liquid breakup may imply topological changes (such as pinching/breaking and puncturing) that cannot be modeled within the continuum assumption of the Navier-Stokes equations
 355 (Gorokhovski and Herrmann, 2008). Still, discretization used in interface capturing methods like VOF, automatically initiates topological changes once the distance between two interfaces can no longer be resolved by the computational mesh. This implies that the smallest resulting liquid structures and the exact moment of the breakup are inherently grid dependent. Nevertheless, this does
 360 not significantly affect droplet sizes that are larger than several cells, i.e., as

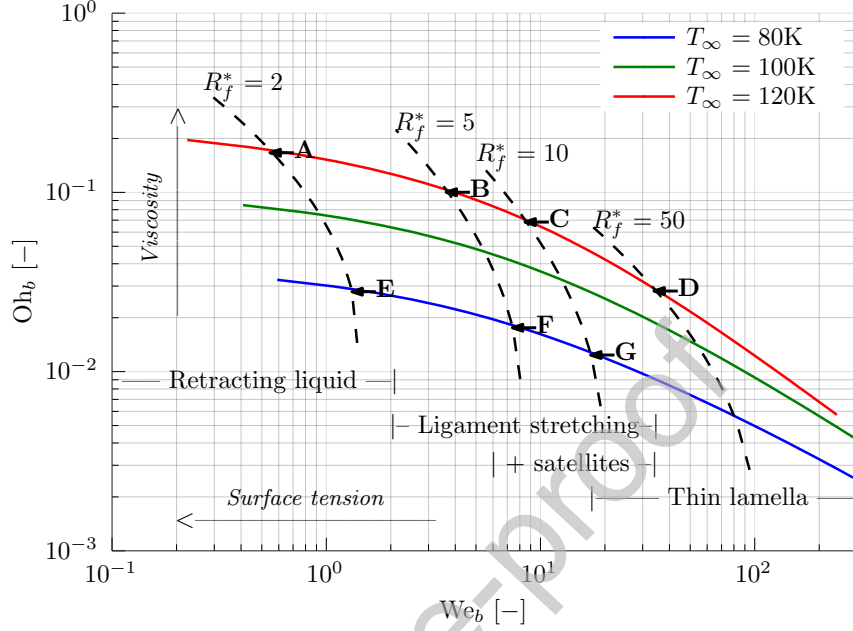


Figure 5: Weber-Ohnesorge diagram to characterize the type of breakup. The correlation to the physical simulation parameters is shown by the T_∞ and $R_f^* = R_f/R_{crit}$ lines, which are based on the RP-e model for superheated LOx at $p_\infty = 10^3$ Pa.

long as the cell is much smaller than the expected (“real”) droplet size. This has been demonstrated in a previous publication (Loureiro et al., 2020) through a mesh convergence study using the present numerical framework. Focusing on the cases with higher We_b , we have observed that mesh convergence can be achieved for the mass-averaged droplet size despite the continued presence of small artificial droplets of the order of the cell size. These small droplets contribute very little to the overall mass. For the case $T_\infty = 120$ K and $R_f^* = 50$ (Case D) we obtain an error of less than 10% in average Sauter mean droplet size when the merging bubble radius R_f is resolved by at least 28 cells. For cases with smaller R_f^* , the breakup dynamics lead to droplets that are much larger relative to R_f and this criterion is therefore relaxed to 20 cells. Cases with higher We_b ($T_\infty = 80$ K, $R_f^* = 50$) were included in the earlier study but are not included here as it was not possible to obtain a converged solution at

Table 2: Summary of setup parameters, dimensionless numbers, mesh resolution and computational cost (estimated) for the series of cases presented.

	Case A	Case B	Case C	Case D	Case E	Case F	Case G
T_∞ [K]	120	120	120	120	80	80	80
p_∞ [Pa]	1×10^3	1×10^3	1×10^3	1×10^3	1×10^3	1×10^3	1×10^3
R_f^-	2	5	10	50	2	5	10
n [$\#/m^3$]	1.89×10^{22}	1.21×10^{21}	1.51×10^{20}	1.21×10^{18}	2.6×10^{16}	1.66×10^{15}	2.08×10^{14}
R_f [m]	2.4×10^{-8}	6.01×10^{-8}	1.2×10^{-7}	6.01×10^{-7}	2.16×10^{-6}	5.4×10^{-6}	1.08×10^{-5}
\dot{R} [m/s]	8.79	15.1	16.9	16.4	2.01	3.03	3.28
D_c [m]	3.96×10^{-8}	9.52×10^{-8}	1.9×10^{-7}	9.47×10^{-7}	3.53×10^{-6}	8.47×10^{-6}	1.69×10^{-5}
We_b [-]	0.545	3.62	8.44	33.8	1.31	7.37	17.1
Oh_b [-]	0.172	0.104	0.0707	0.0291	0.0289	0.0182	0.0128
Re_b [-]	4.28	18.3	41.1	199	39.6	149	323
η [m]	1.62×10^{-8}	1.36×10^{-8}	1.48×10^{-8}	2.26×10^{-8}	2.74×10^{-7}	2.53×10^{-7}	2.84×10^{-7}
Δx [m]	1.2×10^{-9}	3.01×10^{-9}	6.01×10^{-9}	1.9×10^{-8}	1.08×10^{-7}	2.7×10^{-7}	5.4×10^{-7}
$R_f/\Delta x$ [-]	20	20	20	31.7	20	20	20
$\eta/\Delta x$ [-]	13.4	4.51	2.46	1.19	2.53	0.937	0.525
Δt [s]	9.06×10^{-13}	4.85×10^{-12}	1.7×10^{-11}	1.04×10^{-10}	4.42×10^{-10}	2.58×10^{-9}	9.7×10^{-9}
$N_{\Delta x}$ [#]	1.68×10^7	1.68×10^7	1.34×10^8	1.07×10^9	1.68×10^7	1.68×10^7	1.34×10^8
t_{CPU} [core-hours]	5.05×10^3	1.36×10^3	3.38×10^3	1.69×10^4	4.85×10^3	1.18×10^3	2.74×10^3

reasonable computational cost as the estimated mesh size would involve at least
 375 8.6×10^9 grid cells.

The resolution of the Kolmogorov length scale shall serve as a secondary resolution criterion as sufficient resolution of the Kolmogorov length scale ensures adequate resolution of all viscous effects that are crucial during bubble coalescence and subsequent droplet dynamics. For this we define the Reynolds number in the liquid phase as

$$Re_b = \frac{\sqrt{We_b}}{Oh_b} = \frac{\rho_\ell \dot{R}_f 2R_f}{\mu_\ell}, \quad (12)$$

from which the Kolmogorov length scale can be estimated as $\eta = 2R_f/Re_b^{3/4}$. Due to the large ratio of kinematic viscosities, the scale estimated for the gas phase is generally much larger. The mesh resolution used for each case, Δx , is given in Table 2. The mesh resolution factors $R_f/\Delta x$ and $\eta/\Delta x$ demonstrate that the Kolmogorov length scale is over-resolved for most cases when
 380 the criterion of 20 or 30 cells across R_f is used. The final size and estimated computational cost of each case is given by the total number of cells $N_{\Delta x}$, time-

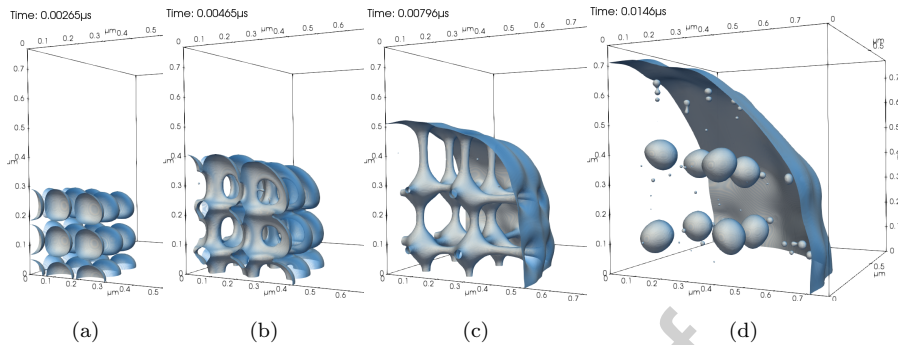


Figure 6: Case B ($T_\infty = 120\text{ K}$, $R_f^* = 5$, $We_b = 3.62$, $Oh_b = 0.104$) – Representative time sequence of the ligament stretching breakup process: (a) Growing bubbles, (b) bubble coalescence, (c) connecting ligaments, (d) resulting droplets. The large surface to the right, top and back corresponds to the interface between the coalesced vapour bubble and the liquid bulk (buffer zone).

step Δt , and the total number of core-hours, t_{CPU} .

6. Breakup patterns

385 We now provide a qualitative classification of the different breakup patterns or modes as given in Fig. 5. The results are rendered using the $f = 0.5$ iso-surface to represent the fluid-vapour interface. This iso-surface acts as a smoothed approximation. The underlying interface is, however, precisely defined by the PLIC reconstruction. Shades are added to help identifying the interface direction.
390

We start with Case B, shown in Fig. 6, as it corresponds to the mechanism that would intuitively be assumed for this kind of bubble arrangement. The sequence shows (a) the array of bubbles after some growth just prior to touching. The bubbles slightly deform as their interfaces approach each other. In (b) the bubbles have touched, forming holes that quickly grow radially as the surface
395 tension force minimizes the total area; in (c) a new stable topology is formed where the main interstitial volumes of liquid are connected by thick ligaments. The liquid momentum due to the initial growth and the continuous evaporation

into the coalesced bubble causes the stretching of these ligaments until they
 400 break. This results in one large droplet per interstitial volume, shown in (d).
 As a consequence of the cubic array arrangement, the size of the droplets is
 approximately equal to the final bubble size (precisely $R_f(6/\pi - 1)^{1/3}$) and it
 can be extrapolated that the number of droplets equals the initial number of
 bubbles. This process is classified as *stretching ligaments* in the classification
 405 chart shown in Fig. 5. This breakup process is in line with the assumption
 promoted by Sher and Elata (1977) and Senda et al. (1994), where the droplet
 number is directly related to the geometric configuration and equals the number
 of spaces in a closely packed bubble arrangement. We demonstrate that it holds,
 however, for the range $2 < We_b < 20$ only. A similar pattern is observed for
 410 Case C, except that for this case satellite droplets are formed (see Fig. 7). These
 small satellite droplets shall not be confused with the much smaller spurious
 droplets observed in Fig. 6 (b) that are artificial, negligible in mass and mesh
 dependent. Case C with a higher We_b leads to relatively large and well resolved
 satellites (at least 10 cells across) in between each pair of the main interstitial
 415 drops. These are a consequence of the connecting ligaments becoming more
 unstable and pinching at both ends instead of breaking at the mid point. The
 low sample size does not allow for detailed statistics, however, a distinctly bi-
 modal droplet size distribution is expected for this regime. Note the larger
 satellite droplets that can be found close to the outer interface. They are well
 420 resolved, but can be related with the use of a continuous liquid buffer zone and
 are therefore neglected in this analysis. An effect of the Ohnesorge number Oh_b
 can be observed for Case F (Fig. 8). The breakup can be classified as being
 within the stretching ligament regime since it has a similar We_b to Cases B and
 C. However, due to the reduced relative strength of viscosity, capillary waves
 425 along the liquid surface are not dissipated resulting in highly irregular oscillating
 droplets.

The sequence shown in Fig. 9 corresponds to Case A which has the low-
 est We_b . With $R_f^* = 2$, this is equivalent to extremely high nucleation rates
 such that bubbles merge soon after nucleation and their final radii are close

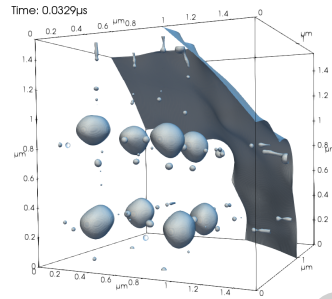


Figure 7: Case C ($T_\infty = 120$ K, $R_f^* = 10$, $We_b = 8.44$, $Oh_b = 0.0707$) – resulting main droplets and satellites

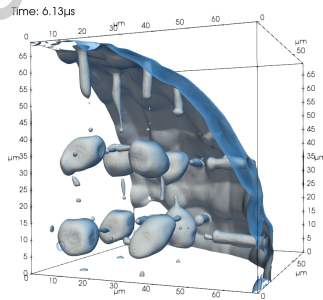


Figure 8: Case F ($T_\infty = 80$ K, $R_f^* = 5$, $We_b = 7.37$, $Oh_b = 0.0182$) – resulting irregular main droplets and satellites

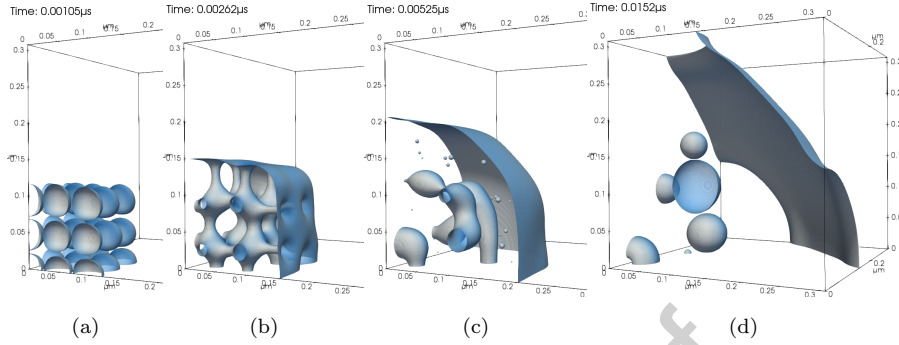


Figure 9: Case A ($T_\infty = 120 \text{ K}$, $R_f^* = 2$, $We_b = 0.545$, $Oh_b = 0.172$) – Representative time sequence of breakup with droplet coalescence: (a) growing bubbles, (b) bubble coalescence, (c) ligament contraction (note some ligaments break while others thicken), (d) coalesced liquid drops (some droplets are bisected by the symmetric boundaries).

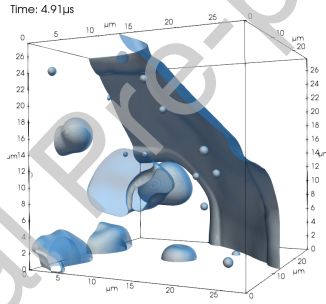


Figure 10: Case E ($T_\infty = 80 \text{ K}$, $R_f^* = 2$, $We_b = 1.31$, $Oh_b = 0.0289$) – Resulting coalesced liquid drops with irregular shapes

430 to R_{crit} . Initially, the bubble coalescence process is similar to Case B. In this case, however, the liquid momentum is not sufficient to complete the breakup and the ligaments pull the interstitial liquid back into larger drops. The same mechanism is observed for Case E shown in Fig. 10. The latter corresponds to a much lower Oh_b and again shows more irregular droplet shapes as a result of the reduced viscous dissipation. We define this regime as *retracting liquid* 435 for $We_b < 2$. The naming indicates that the surface tension forces dominate over the liquid momentum, retracting the still connected liquid fluid elements from the spaces between the bubbles towards (eventually) spherical drops that

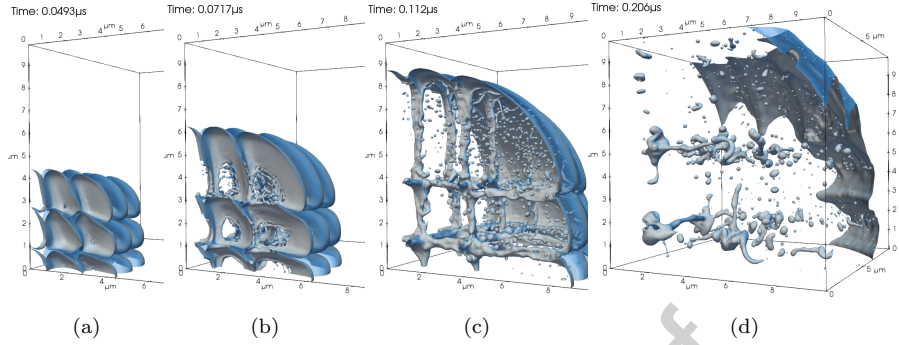


Figure 11: Case D ($T_\infty = 120 \text{ K}$, $R_f^* = 50$, $We_b = 33.8$, $Oh_b = 0.0291$) – Time sequence of the breakup process with the formation of thin lamellae: (a) deformed bubbles after initial growth, (b) thin lamella burst and retraction, (c) weak ligament structure and droplets resulting from lamella bursting (d) final droplet formation resulting from ligament breakup.

will be rather large relative to the bubble size. The critical We_b for which the transition to the momentum dominated regime occurs is not defined precisely by the parameter matrix used here. In the light of our modelling assumptions and boundary conditions it suffices to state here that a transition exists and will most likely occur within a narrow range of $We_b \in]1.3; 2[$. Note that for a perfectly aligned bubble array (no random offset of bubble centers) droplet coalescence tends to be hindered since all ligaments pull with exact the same strength until they break simultaneously. As this is rather unrealistic the random offsets described in Sec. 4.2 were introduced.

Finally, we turn our attention to the *thin lamella* regime found for large We_b cases located on the right of Fig. 5. The existence of thin lamellae during breakup is demonstrated by Case D (cf. Fig. 11). After the initial growth the surface tension force is not sufficient to maintain a spherical bubble shape. This leads to highly deformed bubbles, shown in Fig. 11 (a), that naturally develop a flat surface when colliding with their neighbours. Thin films of liquid are thus trapped between the bubbles. They become increasingly thinner as they continue to evaporate and are stretched by the growing bubbles. When a critical thickness is reached, the lamellae are either punctured and start retracting, or

burst into many small droplets, shown in (b). The result is again a structure of connected ligaments, shown in (c), surrounded by the small droplets which will be further discussed below. Contrary to previous cases the surface tension force is very weak, causing the ligaments to break simply due to vorticity and other fluctuations in the flow. Also, the volume of liquid left in the main interstices is much smaller leading to smaller "main" droplets relative to the final bubble size, when compared with other cases. As a result, there is a wide distribution of droplet sizes and irregular ligament shapes, shown in (d).

The last case studied, Case G (Fig. 12), is a transition case between the stretching ligaments and the thin lamella regimes. The characteristics of bubble

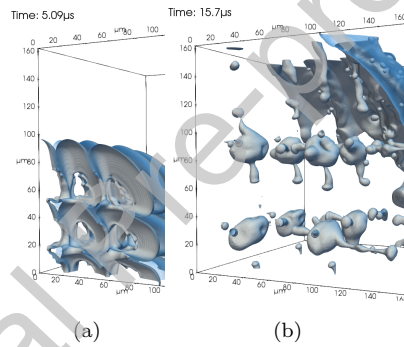


Figure 12: Case G ($T_\infty = 80$ K, $R_f^* = 10$, $We_b = 17.1$, $Oh_b = 0.0128$) – (a) lamella retraction (b) resulting irregular main droplets and satellites.

merging are similar to Case D as thin lamellae form, puncture and retract. The lamella retracts with the formation of a stable rim shedding no droplets or only very few droplets in the process (Fig. 12 (a)). This is because the lamella is thicker around the initial puncture point when compared to Case D. The final droplet formation, shown in Fig. 12 (b) is similar to Case F, since the weak ligaments break into satellite droplets and main interstitial drops, the latter being very irregular due to the low Oh_b number.

For liquids with low viscosity, the dynamics of lamella retraction depend on the film thickness as determined by the Taylor-Culick velocity (Taylor, 1959)

and have been analysed by Agbaglah et al. (2013). They show that droplets may form due to the formation of liquid fingers as the rim becomes unstable while retracting. Such dynamics can also be captured here in transitional cases such as Case G. However, for higher We_b cases (including Case D), the lamellae become thinner and possible mesh effects need to be considered. In all cases analysed the bubble coalescence process is initiated when the distance between interfaces is no longer resolved with the VOF method. At low We_b this affects the exact timing of the initial puncture only, but the subsequent dynamics do not change. For the cases in the thin lamella regime, however, the resolution determines the thickness of the lamella and consequently its retraction velocity. The formation of a round rim at the edge of the lamella implies a thin neck region just behind it. This neck may become under-resolved, causing the rim to detach from the lamella and forming a series of parallel ligaments that then break into small droplets as seen in Fig. 11 (d). In zones where the thickness of the liquid film is nearly uniform, the whole structure becomes under-resolved at the same time and bursts into many small droplets. For both cases (rim detachment and nearly uniform thin film), a large number of very small droplets is observed (see top-right of Fig. 11 (c)). These droplets are likely to be mesh dependent as break-up dynamics will be influenced by interference of surface tension forces from both sides of the lamella (Liu and Bothe, 2016). The effect has been discussed in more detail in Loureiro et al. (2020). There, we concluded that for the conditions of Case D the formation of non-physical droplets during lamella retraction cannot be avoided, but their size is very small relative to the droplets that naturally form under these flow conditions (compare Fig. 11 (c) and (d)). Therefore, all results hold and meaningful statistics can be extracted particularly in terms of the weighted means such as the Sauter diameter. It should also be noted that in a more realistic flow with a random nucleation and thus, random bubble arrangement, the formation of these extremely thin and flat lamellae is less likely to occur.

Additional cases with higher We_b and lower Oh_b (towards the bottom-right corner of Fig. 5) have been tested showing similar breakup patterns and mesh ef-

fects. However, the physical droplet size expected is smaller and becomes harder to distinguish from mesh-dependent droplets. In these regions of the classification diagramme, mesh convergence could not be reached for reasonably sized meshes (up to 1 billion cells). Furthermore, the reduced viscosity associated with low Oh_b implies a larger Re_b and a small Kolmogorov length scale relative to the bubble size. This marks the transition to a turbulence-dominated breakup regime that lies beyond the scope of this work and should be studied in the context of a jet (e.g. Ertl et al. (2018)) or shear layer.

7. Discussion

Considering the current knowledge of the microscopic processes that drive flash atomization, some assumptions and conjectures have been invoked to establish a regime diagramme of the bubble breakup processes. Here, we summarize and discuss all assumptions and approximations made:

1. The simulation domain is very small relative to the jet diameter and is far from the injector walls.
2. The timescale of the breakup process is very short compared with the characteristic time of the jet.
3. The flow is continuous in each phase.
4. Molecular-scale forces and Marangoni effects are neglected.
5. The evaporation mass flux is uniform and based on spherical bubble growth of bubbles of size R_f . Also, the vapour temperature and pressure are assumed to be uniform and in equilibrium with the liquid-vapour interface temperature.
6. Bubbles have equal size. They are homogeneously distributed within the control volume. Liquid temperature and pressure (p_∞, T_∞) are uniform and remain constant.
7. Both, the liquid and the vapour are incompressible fluids. The evaporation rate is unaffected by instantaneous pressure fluctuations such as propagating pressure waves.

8. The boundary layer surrounding the bubbles is thin and there is no bubble interaction through heat conduction.

9. The bubbles are arranged in cubic lattice arrays.

10. Computations do not include secondary atomization.

540 Assumptions 1 to 4 impose upper and lower limits for the physical size of the simulation domain and the bubbles. The assumption of small length and time scales relative to the jet (1 and 2) are necessary to ensure that the breakup process is not influenced by macroscopic gradients of velocity or thermodynamic conditions. For the high temperature cases ($T_\infty = 120\text{ K}$) the length scales for
 545 the breakup are of the order of $0.1\ \mu\text{m}$ to $1\ \mu\text{m}$, and the whole breakup process lasts between 10 ns to $0.5\ \mu\text{s}$. This can be compared with a typical injection condition of the DLR flash atomization experiments where fluid is injected with a bulk exit velocity of $\mathcal{O}(10\text{ m/s})$ through a nozzle of $\mathcal{O}(0.1 - 1\text{ mm})$ nozzle diameter. This gives in a characteristic jet time scale of $\mathcal{O}(10 - 100\ \mu\text{s})$ and
 550 confirms that the flashing process is very fast and localized and the assumptions hold. For the low temperature cases ($T_\infty = 80\text{ K}$), both time and length scales increase by a factor of 100, when compared with the high temperature cases. For the largest R_f^* this yields a domain size comparable to the diameter of a small injector. For such cases, the macroscopic jet flow as well as hydrodynamic
 555 effects associated with large Reynolds numbers may affect breakup and results should be interpreted with care if injectors with small diameters are used.

The extremely small length scales associated with the high temperature cases, when the bubble size is close to the critical radius, could potentially violate the continuity assumption of the Navier-Stokes equations (assumption
 560 3). For all cases and both phases, the Knudsen number (defined as the ratio of the mean free path in the vapour and the bubble radius) is of the order of $\mathcal{O}(10^{-2})$ or smaller and the continuity assumption holds. Still, referring to assumption 4, molecular scale effects can be present but are neglected. These include the physics of film drainage and rupture and Marangoni effects.
 565 Also, thermo-capillary convection could potentially influence the details of the

breakup process but is not included at this point since temperature gradients are not resolved. We presume that the resolved dynamic effects driven by the liquid momentum and evaporation dominate the breakup process and that molecular effects are small and do not affect the conclusions drawn here.

570 Assumption 5 refers to the RP-e solution that has been used to determine the evaporation rate as a function of the initial conditions (T_∞ , p_∞ and R^*) and the characteristic key quantities (We_b , Oh_b and Re_b). This does not impede the use of simpler models (such as Scriven (1959) or Mikic et al. (1970)) that hold for specific stages of bubble growth and introduces further assumptions. 575 The one-dimensional numerical solution used here, however, is valid for all stages of bubble growth and can be further extended to cover more complex dynamics. Namely, if a precise pressure profile was known at the nozzle exit (Fig. 1), the RP-e system can be solved with varying p_∞ and, thus, provide a more accurate estimate of the bubble growth rate. Note that here we use a constant evaporation rate for the DNS that is obtained from the RP-e solution 580 for the given R_f . The DNS growth rates are therefore not accurate for the initial bubble growth. This does not, however, unduly influence the breakup regime as the latter is dominated by the dynamics at the time when the bubbles merge (Loureiro et al., 2018).

585 The use of the RP-e model also leads to approximation 6, which implies a uniform bubble distribution, temperature and pressure. This implies that all the bubbles have the same size when merging and that one set of growth rate and properties obtained from the RP-e solution approximates the dynamics of all bubbles equally well. The assumption is consistent with 1 and 2 and therefore 590 holds (at least for the high temperature cases). Furthermore, this approximation implies an appropriate simplification if the results were to be used as sub-grid scale data in the context of large scale LES or RANS, where only averaged properties within a cell are known.

Approximations 7 and 8 relate to the level of physical detail included in the 595 simulations. Compressibility effects (7) are particularly important in the vapour phase. Although they are not captured in the DNS, they are implicitly included

in the calibrated evaporation rate as detailed in Sec. 3. In the liquid phase, compressibility is negligible considering low Mach number (under 0.1) for the peak velocity expected. Still, the effect of propagating pressure waves is noteworthy.

600 Using a fully compressible approach, Dietzel et al. (2019a) showed that pressure waves induced by bubble expansion lead to a pressure gradient within the jet. This result can be used in future work to calibrate the bubble growth rate as a function of space and time within the DNS domain. Additionally, Dietzel et al. (2019a) demonstrated that along a given direction towards the free surface of the jet, the number of bubbles that experience a significant growth is limited,

605 which can justify the use of a small number of bubbles in the domain. Naturally, as the bubbles grow and the liquid breaks up, this free interface propagates towards the centre of the jet, leading to a complete atomization.

The assumption of constant temperature in the liquid (assumption 8) is not

610 a necessary condition for the current approach. This simplification is justified when the thermal boundary layer surrounding the bubbles is very thin. The existence of thin boundary layers is commonly used (Prosperetti, 2017) and RP-e solutions suggest maximum thicknesses of $\delta_{th} \sim \mathcal{O}(0.25R)$ for the high temperature cases. Resolving these layers may become useful if an additional energy

615 transport equation is solved and the cooling of the liquid was to be deduced for the computation of thermo-capillary effects and a temperature distribution of the resulting droplets. Here, this would not represent an advantage over the RP-e solution as the DNS solution would also need to capture variations in vapour density (cf. Fig. 3) which would require a compressible solver.

620 The use of a cubic lattice array (approximation 9) leads to a canonical setup that allows for a reasonably simple analysis of the fluid dynamics, the breakup process, the repeatability of results and an easy parametrization of the case setups. Since the breakup dynamics depend on the ratio between the different forces (characterized by We_b and Oh_b) similar types of breakup patterns can

625 be expected for any type of bubble arrangement where these forces exist. It is worth noting that the cubic lattice array allows for some interstitial regions to remain connected and ligaments can form once the bubbles start to coalesce.

This seems reasonable (and more comparable to a realistic random bubble distribution) but is in contrast with densely packed bubble arrays used by other
630 researchers (Sher and Elata, 1977; Senda et al., 1994). There, the formation of such interconnecting ligaments is artificially suppressed and many characteristics of the breakup dynamics observed here would not be present. The ligament suppression may for example lead to a near to instantaneous breakup when the bubbles touch resulting in - rather unlikely - droplet numbers and sizes equal
635 to the spaces in between the bubbles in a densely packed array. Also note that the use of setups with regular bubble arrays is not a necessary condition for the methods used and future studies shall employ randomized bubble arrangements from which statistical data on droplet size and velocity distributions can be extracted.

640 Lastly, a comparison of length scales and the droplet sizes in the different regimes suggests that secondary atomization may be possible due to bubble formation within the larger droplets that continue to be superheated. Such scenarios represent typical micro explosion regimes and are not covered here (cf. approximation 10) but could easily be analysed by very similar set-ups.
645 Then, the bubble cluster would be initialized within a larger spherical droplet surrounded by vapour that would also extend throughout the buffer zone. Similar to present computations, bubble growth and droplet atomization would be governed by the local thermodynamic conditions within the droplet.

8. Conclusions

650 In this work a fully numerical approach is used to investigate the primary breakup processes occurring at the microscopic scales associated with flash-boiling atomization. The conditions are representative of the injection of liquid oxygen in the low pressure combustion chamber of a rocket thruster in space. Simulations of a series of representative test cases are performed with fully
655 resolved interfaces using the volume of fluid method and PLIC. The DNS focuses on the hydrodynamic aspects while the dependent thermodynamic variables are

calibrated according to a model for bubble growth in superheated liquid. A series of breakup modes and droplet formation patterns are identified for a range of initial conditions. It is shown that the type of breakup is mainly determined
660 by a Weber number that strongly correlates with the bubbles size relative to its critical radius at the time of breakup (i.e. growth factor since nucleation) and, therefore, the bubble number density. This observation holds across the range of liquid temperatures, even though an order of magnitude change in the physical length scale is realized by the different test cases. In turn, the liquid temperature
665 strongly influences the relative strength of the viscous dissipation (given by the Ohnesorge number). Within the different breakup regimes identified, only one regime is compatible with the conventional assumption that droplets form from the interstitial volumes in a closely packed bubble array, and that their size can be estimated as suggested in the literature. For higher bubble number densities,
670 surface tension forces dominate leading to the retraction and merging of adjacent and elongated liquid volumes toward spherical bubbles. For lower densities when bubbles merge at a larger relative size, large numbers of much smaller droplets are formed due to the larger Weber numbers. These observations provide a first insight into the mechanics of the primary atomization process. This has
675 never before been quantified. While the results presented here are of qualitative nature only, it sets clear limits to current modeling strategies and shall prompt further research into adequate droplet statistics after breakup considering the possible range of flash atomization conditions found in the relevant applications such as the ignition of upper-stage rocket engines and reaction control systems.

680 **Acknowledgements**

Some of the simulations presented in this work were performed on the CRAY XC40 Hazel-Hen of the High Performance Computing Center Stuttgart (HLRS). This work is part of the HAoS-ITN project and has received funding from the European Union's Horizon 2020 research and innovation programme under the
685 Marie Skłodowska-Curie grant agreement No 675676 (DL). We also acknowl-

edge funding by the Deutsche Forschungsgemeinschaft (DFG, German Research Foundation) - Project SFB-TRR 75, Project number 84292822 (JR, AK, BW) and by the UK's Engineering and Physical Science Research Council support through the grant EP/S001824/1 (KV).

690 **References**

- Agbaglah, G., Josserand, C., Zaleski, S., 2013. Longitudinal instability of a liquid rim. *Physics of Fluids* 25, 022103. doi:10.1063/1.4789971.
- Ashgriz, N., 2011. *Handbook of atomization and sprays: theory and applications*. Springer Science & Business Media.
- 695 Bar-Kohany, T., Levy, M., 2016. State of the art review of flash-boiling atomization. *Atomization and Sprays* 26, 1259–1305.
- Bardia, R., F. Trujillo, M., 2018. Assessing the physical validity of highly-resolved simulation benchmark tests for flows undergoing phase change. *International Journal of Multiphase Flow* 112. doi:10.1016/j.ijmultiphaseflow.2018.11.018.
- 700 Bell, I.H., Wronski, J., Quoilin, S., Lemort, V., 2014. Pure and pseudo-pure fluid thermophysical property evaluation and the open-source thermophysical property library coolprop, in: *Industrial & Engineering Chemistry Research*. volume 53, pp. 2498–2508. doi:10.1021/ie4033999.
- 705 Calay, R., Holdo, A., 2008. Modelling the dispersion of flashing jets using cfd. *Journal of Hazardous Materials* 154, 1198–1209.
- Carey, V., 1992. *Liquid-vapor phase-change phenomena*. Taylor & Francis Inc., Bristol PA, USA.
- Cleary, V., Bowen, P., Witlox, H., 2007. Flashing liquid jets and two-phase droplet dispersion: I. experiments for derivation of droplet atomisation correlations. *Journal of Hazardous Materials* 142, 786 – 796. doi:10.1016/j.jhazmat.2006.06.125.

- Dietzel, D., Hitz, T., Munz, C.D., Kronenburg, A., 2019a. Numerical simulation of the growth and interaction of vapour bubbles in superheated liquid jets. *International Journal of Multiphase Flow* 121, 103 – 112. doi:10.1016/j.ijmultiphaseflow.2019.103112.
- 715
- Dietzel, D., Hitz, T., Munz, C.D., Kronenburg, A., 2019b. Single vapour bubble growth under flash boiling conditions using the hllp riemann solver. *International Journal of Multiphase Flow* 116, 250–269. doi:10.1016/j.ijmultiphaseflow.2019.04.010.
- 720
- Eisenschmidt, K., Ertl, M., Gomaa, H., Kieffer-Roth, C., Meister, C., Rauschenberger, P., Reitzle, M., Schlottke, K., Weigand, B., 2016. Direct numerical simulations for multiphase flows: An overview of the multiphase code FS3D. *Journal of Applied Mathematics and Computation* 272, 508–517.
- 725
- Ertl, M., Reutzsch, J., Nägel, A., Wittum, G., Weigand, B., 2018. Towards the implementation of a new multigrid solver in the DNS code FS3D for simulations of shear-thinning jet break-up at higher reynolds numbers, in: *High Performance Computing in Science and Engineering ' 17*, Springer International Publishing, pp. 269–287.
- 730
- Gaertner, J.W., Rees, A., Kronenburg, A., Sender, J., Oswald, M., Lamanna, G., 2020. Numerical and Experimental Analysis of Flashing Cryogenic Nitrogen. *International Journal of Multiphase Flow*, accepted.
- 735
- Gaertner, J.W., Rees, A., Kronenburg, A., Sender, J., Oswald, M., Loureiro, D., 2019. Large Eddy Simulation of Flashing Cryogenic Liquid with a Compressible Volume of Fluid Solver, in: *ILASS–Europe 2019, 29th Conference on Liquid Atomization and Spray Systems*.
- Gorokhovski, M., Herrmann, M., 2008. Modeling primary atomization. *Annual Review of Fluid Mechanics* 40, 343–366. doi:10.1146/annurev.fluid.40.111406.102200.

- 740 Hurlbert, E., Applewhite, J., Nguyen, T., Reed, B., Baojiong, Z., Yue, W., 1998. Nontoxic Orbital Maneuvering and Reaction Control Systems for Reusable Spacecraft. *Journal of Propulsion and Power* 14, 676–687. doi:10.2514/2.5330.
- Karathanassis, I., Koukouvinis, P., Gavaises, M., 2017. Comparative evaluation
745 of phase-change mechanisms for the prediction of flashing flows. *International Journal of Multiphase Flow* 95, 257–270.
- Lafaurie, B., Nardone, C., Scardovelli, R., Zaleski, S., Zanetti, G., 1994. Modelling merging and fragmentation in multiphase flows with surfer. *Journal of Computational Physics* 113, 134 – 147.
- 750 Lamanna, G., Kamoun, H., Weigand, B., Manfretti, C., Rees, A., Sender, J., Oschwald, M., Steelant, J., 2015. Flashing behavior of rocket engine propellants. *Atomization and Sprays* 25, 837–856.
- Lamanna, G., Kamoun, H., Weigand, B., Steelant, J., 2014. Towards a unified treatment of fully flashing sprays. *International Journal of Multiphase Flow*
755 58, 168 – 184.
- Lecourt, R., Barricau, P., Steelant, J., 2009. Spray velocity and drop size measurements in flashing conditions. *Atomization and Sprays* 19, 103–133. doi:10.1615/AtomizSpr.v19.i2.10.
- Lee, H.S., Merte, H., 1996. Spherical vapor bubble growth in uniformly super-
760 heated liquids. *International Journal of Heat and Mass Transfer* 39, 2427–2447.
- Lee, J., Madabhushi, R., Fotache, C., Gopalakrishnan, S., Schmidt, D., 2009. Flashing flow of superheated jet fuel. *Proceedings of the Combustion Institute* 32, 3215 – 3222. doi:10.1016/j.proci.2008.06.153.
- 765 Levy, M., Levy, Y., Sher, E., 2014. Spray structure as generated under homogeneous flash boiling nucleation regime. *Applied Thermal Engineering* 73, 416 – 423. doi:10.1016/j.applthermaleng.2014.08.008.

- Liu, M., Bothe, D., 2016. Numerical study of head-on droplet collisions at high weber numbers. *Journal of Fluid Mechanics* 789, 785–805. doi:10.1017/jfm.2015.725.
- 770
- Loureiro, D., Reutzsch, J., Dietzel, D., Kronenburg, A., Weigand, B., Vogiatzaki, K., 2018. DNS of multiple bubble growth and droplet formation in superheated liquids, in: 14th International Conference on Liquid Atomization and Spray Systems ,Chicago, IL, USA. doi:10.18419/opus-10342.
- 775
- Loureiro, D., Reutzsch, J., Kronenburg, A., Weigand, B., Vogiatzaki, K., 2020. Towards full resolution of spray breakup in flash atomization conditions using DNS, in: High Performance Computing in Science and Engineering ' 20, Springer International Publishing. (accepted).
- Luo, M., Haidn, O.J., 2016. Characterization of Flashing Phenomena with Cryogenic Fluid Under Vacuum Conditions. *Journal of Propulsion and Power* 32, 1253–1263. doi:10.2514/1.B35963.
- 780
- Manfretti, C., 2014. Laser Ignition of an Experimental Cryogenic Reaction and Control Thruster: Pre-Ignition Conditions. *Journal of Propulsion and Power* 30, 925–933.
- 785
- Mikic, B., Rohsenow, W., Griffith, P., 1970. On bubble growth rates. *International Journal of Heat and Mass Transfer* 13, 657 – 666. doi:10.1016/0017-9310(70)90040-2.
- Navarro-Martinez, S., 2014. Large eddy simulation of spray atomization with a probability density function method. *International Journal of Multiphase Flow* 63, 11–22.
- 790
- Oxtoby, D.W., 1992. Homogeneous nucleation: theory and experiment. *Journal of Physics: Condensed Matter* 4, 7627–7650. doi:10.1088/0953-8984/4/38/001.
- Oza, R.D., Sinnamon, J.F., 1983. An experimental and analytical study of flash-boiling fuel injection. *SAE Transactions* 92, 948–962.
- 795

- Prosperetti, A., 2017. Vapor bubbles. *Annual review of fluid mechanics* 49.
- Razzaghi, M., 1989. Droplet size estimation of two-phase flashing jets. *Nuclear Engineering and Design* 114, 115 – 124. doi:10.1016/0029-5493(89)90130-1.
- 800 Rees, A., Araneo, L., Salzmann, H., Kurudzija, E., Suslov, D., Lamanna, G., Sender, J., Oswald, M., 2019. Investigation of Velocity and Droplet Size Distributions of Flash Boiling LN2-Jets With Phase Doppler Anemometry, in: *ILASS-Europe 2019, 29th Conference on Liquid Atomization and Spray Systems*.
- 805 Rider, W.J., Kothe, D.B., 1998. Reconstructing volume tracking. *Journal of computational physics* 141, 112–152.
- Rieber, M., 2004. Numerische Modellierung der Dynamik freier Grenzflächen in Zweiphasenströmungen. Ph.D. thesis. Universität Stuttgart.
- Robinson, A., Judd, R., 2004. The dynamics of spherical bubble growth. *International Journal of Heat and Mass Transfer* 47, 5101 – 5113. doi:10.1016/j.ijheatmasstransfer.2004.05.023.
- 810 Schlottke, J., Weigand, B., 2008. Direct numerical simulation of evaporating droplets. *Journal of Computational Physics* 227, 5215–5237.
- Scriven, L., 1959. On the dynamics of phase growth. *Chemical Engineering Science* 10, 1 – 13. doi:10.1016/0009-2509(59)80019-1.
- 815 Senda, J., Hojyo, Y., Fujimoto, H., 1994. Modeling on atomization and vaporization process in flash boiling spray. *JSAE Review* 15, 291 – 296.
- Sher, E., Bar-Kohany, T., Rashkovan, A., 2008. Flash-boiling atomization. *Progress in Energy and Combustion Science* 34, 417–439.
- 820 Sher, E., Elata, C., 1977. Spray formation from pressure cans by flashing. *Industrial & Engineering Chemistry Process Design and Development* 16, 237–242.

- Shneider, M.N., Pekker, M., 2019. Surface tension of small bubbles and droplets and the cavitation threshold. arXiv preprint arXiv:1901.04329 .
- 825 Shusser, M., Ytrehus, T., Weihs, D., 2000. Kinetic theory analysis of explosive boiling of a liquid droplet. *Fluid Dynamics Research* 27, 353 – 365. doi:10.1016/S0169-5983(00)00015-0.
- Taylor, G.I., 1959. The dynamics of thin sheets of fluid ii. waves on fluid sheets. *Proceedings of the Royal Society of London. Series A. Mathematical and*
830 *Physical Sciences* 253, 296–312. doi:10.1098/rspa.1959.0195.
- Thompson, A.S., Heister, S.D., 2016. Characteristics Of Flashing Flows Within a High Aspect Ratio Injector. *Atomization and Sprays* 26, 633–658.
- Zeng, Y., Lee, C.F.F., 2001. An atomization model for flash boiling sprays. *Combustion Science and Technology* 169, 45–67.

Declaration of interests

The authors declare that they have no known competing financial interests or personal relationships that could have appeared to influence the work reported in this paper.

The authors declare the following financial interests/personal relationships which may be considered as potential competing interests:

Journal Pre-proof